

Application of the Singular Spectrum Analysis on electroluminescence images of thin-film photovoltaic modules

Evgenii Sovetkin and Bart E. Pieters

Abstract This paper discusses an application of the singular spectrum analysis method (SSA) in the context of electroluminescence (EL) images of thin-film photovoltaic (PV) modules. We propose an EL image decomposition as a sum of three components: global intensity, cell, and aperiodic components. A parametric model of the extracted signal is used to perform several image processing tasks. The cell component is used to identify interconnection lines between PV cells at a sub-pixel accuracy, as well as to correct incorrect stitching of EL images. Furthermore, an explicit expression of the cell component signal is used to estimate the inverse characteristic length, a physical parameter related to the resistances in a PV module.

1 Introduction

There has been an increasing interest in automated image analysis of spatially resolved characterisation methods for photovoltaic (PV) modules such as electroluminescence (EL) Demant et al. (2018); Deitsch et al. (2018, 2019); de Oliveira et al. (2019); Karimi et al. (2019); Sovetkin and Steland (2019); Sovetkin et al. (2021, 2020). Such automated image analysis aims at quality control of modules and is thus of great interest for manufacturers, PV system owners, and insurance companies, as it allows for a systematic inspection of a large number of modules, both prior and after installation.

Electroluminescence is a commonly used imaging technique for PV modules. It relies on the reciprocal operation of the photovoltaic module as a light-emitting diode, so instead of generating an electric current from light, an electric current is

Evgenii Sovetkin and Bart E. Pieters
IEK5-Photovoltaik, Forschungszentrum Jülich, 52425 Germany
e-mail: e.sovetkin@fz-juelich.de

driven through the solar cell, which then emits light. As generating electricity and emitting light are reciprocal processes, one process reveals much about the other. Electroluminescence (EL) images provide spatially resolved information on the solar module and is commonly used to locate and identify defects in the device or extract other (local) solar cell properties.

In this paper our focus lies on EL images of thin-film PV modules. For thin-film technology, unlike for a more common crystalline silicon, little is known about shapes and appearances of defects in EL images. For the crystalline silicon PV modules there exists a well-established catalogue of defects visible in EL images (see Köntges et al. (2015)), whereas such a catalogue does not exist for thin-film modules.

To study defects in EL images, it is important to find a compact way to represent EL image data. This paper proposes such an approach and considers several image processing algorithms for EL images of thin-film PV modules that are based on the singular spectrum analysis (SSA). Our contributions here are manifold.

Firstly, a specific grouping in the SSA algorithm decomposes an EL image into several components: global intensity variation component, local periodic intensity component (or cell component), and a residual image that contains various local aperiodic features. We argue that each of these components has a different physical origin.

Secondly, the extracted components of an EL image can be approximated by a parametric model, that represents an EL image as a small dimensional vector, and hence our methods can also be considered as a dimensionality reduction technique. Furthermore, the parametric model of the cell components is used to estimate the position of the interconnection line between individual PV cells. Our algorithm features symbolic differentiation and estimates positions of the interconnection lines at a sub-pixel accuracy. A similar technique is used in the estimation of the inverse characteristic length, a physical characteristic of a PV module that equals the square of the ratio between different resistances in a module.

Lastly, the cell component signal is used to estimate a non-linear transformation of an image to adjust an incorrectly stitched image.

The rest of the paper is organised as follows. Section 2 reviews the methods and the corresponding literature used in this paper. Section 3 describes the data used in the project. The main contribution of this paper is given in Section 4, which focuses on various applications of SSA to the EL images of thin-film modules. Lastly, the paper is concluded in Section 5.

2 Methods overview

This section describes the methods used in this paper and overviews related literature. Our main tool is the singular spectrum analysis method (SSA).

The history of SSA can be traced to the works of Broomhead and King (1986), where an SSA-like method was established and applied in the context of nonlinear dynamics for the purpose of reconstructing the attractor of a system from measured

time series. Further, in the context nonlinear dynamical system, SSA can be also used for phase space reconstruction algorithm, Elsner and Tsonis (1996).

The so-called “Caterpillar” methodology is a parallel development of SSA that originated in the former Soviet Union, especially in Saint Petersburg, independently of the mainstream SSA work in the West, Danilov and Zhigljavsky (1997). This methodology became known to the rest of the world more recently. “Caterpillar-SSA” Golyandina et al. (2001), emphasises the concept of separability, a concept that leads, for example, to specific recommendations concerning the choice of the SSA parameters.

Originally, the SSA method was applied to the one-dimensional time-series data. In fact, by now, it is not easy to find an applied area related to the analysis of temporal data, where one-dimensional SSA is not being applied. To name a few applications, the method found its way to the analysis of climate and atmospheric data, Vautard and Ghil (1989); Fraedrich (1986), to meteorological data, Weare and Nasstrom (1982), as well as to the marine science, Colebrook (1982). Lima et al. (2016) used SSA for gap filling in precipitation data. This method has been also applied in the financial sector to discover hidden economic cycles, Sella et al. (2016). Groth and Ghil (2015) used a multivariate extension of SSA and defined a Procrustes test to the analysis of interannual variability in the North Atlantic sea surface temperature. For further references to various applications of SSA in time-series analysis see Zhigljavsky (2010); Golyandina et al. (2018).

More recently, SSA was also used to analyse digital images and other objects that are not necessarily of planar or rectangular form. This particular development is utilised in this paper. Rodriguez-Aragon and Zhigljavsky (2010), used SSA to define a distance between images with a possible application in face verification. In Zabalza et al. (2014, 2015); Qiao et al. (2016) the 1D-/2D-SSA variants were used in the context of hyperspectral images for the purpose of denoising, feature extraction, and classification tasks. In Mamou and Feleppa (2007) SSA was applied in the context of ultrasonic imaging for improving the imaging of brachytherapy seed. In application related to geoscientific data, 2D-SSA was utilised for gap-filling, Zscheischler et al. (2014). 2D-SSA was also applied in texture classification Monadjemi (2004), seismology Trickett (2008), gene expression Holloway et al. (2011), and medical imaging Shin et al. (2014).

In our application of the 2D-SSA, we utilise the ability of the method to separate signal into trend and periodic components. Further, we use the parametric form of the extracted signal to perform various image processing tasks.

In order to explain our algorithms, we give a review of necessary theory in the following subsections. The SSA algorithm is reviewed in Section 2.1. SSA itself is non-parametric, however, a parametric model can be given to describe the extracted signal. There are two sets of parameters to be estimated in the model. The ESPRIT method (Section 2.2) estimates frequencies and damping factors of a signal, where the least squares provides an estimation of the amplitude and phases (Section 2.3). Lastly, remarks on implementation and comparison to similar methods are discussed in Section 2.4.

2.1 SSA

Singular Spectrum Analysis (SSA) is a model-free time series analysis method that belongs to the so-called subspace methods, Van Der Veen et al. (1993). In subspace methods, a signal estimation is performed by taking a certain linear subspace. SSA can also be considered as a low-rank approximation method, Markovsky (2018).

The general theory of SSA for one-dimensional time series is elaborated in Golyandina et al. (2001). Golyandina et al. (2018) provide more updated information on extensions with a strong focus on applications.

The output of SSA-like methods is a decomposition of an observed signal x (e.g. a time series, a multivariate time series or an image) into a sum of identifiable components:

$$x = x_1 + \dots + x_n. \quad (1)$$

Among all SSA-like methods, the following four common algorithm steps can be isolated.

1. **Embedding.** The original signal x (e.g. time series or an image) is mapped into a matrix \mathbf{X} , that is called a *trajectory matrix*.
The embedding is parametrised by a single parameter denoted by L (a number or a vector).
2. **Decomposition.** The second step consists of the decomposition of the trajectory matrix \mathbf{X} into a sum of matrices of rank 1.
Often the singular value decomposition (SVD) is used for this purpose, which is an optimal rank-one matrix decomposition in the Frobenius norm sense.
3. **Grouping.** The third step is a grouping of the decomposition components. At the grouping step, the elementary rank-one matrices are grouped and summed within groups.
The grouping algorithm step is often semi-automatic and depends on the type of data and application.
4. **Reconstruction.** The grouped components are not necessarily valid trajectory matrices. Hence a projector operator to trajectory matrix space is applied on the grouped components, resulting in the final signal decomposition (1).

In this paper, we utilise the 2D-SSA variant of the algorithm, Golyandina and Usevich (2009, 2010); Golyandina et al. (2015). For this variant, the trajectory matrix is a Hankel-block-Hankel matrix and the corresponding embedding is parametrised by a two-dimensional parameter $L = (L_1, L_2) \in \mathbb{N}^2$. The decomposition is performed with SVD, and the reconstruction projection operator is a 2-step diagonal averaging procedure. The precise forms of the embedding, SVD, and reconstruction projection operator are provided in the Appendix.

The grouping step of the SSA algorithm determines the form of the final signal decomposition. A typical SSA decomposition of a signal is the decomposition into a slowly-varying trend, regular oscillations, and noise. An important notion in the SSA theory is the notion of *the signal of finite rank*. This notion allows us to classify and group together rank-one matrices into a trend, oscillations, and noise components.

Informally, finite rank signals are those that have a trajectory matrix of a finite rank (see a formal definition in the Appendix). 2D-SSA produces a class of signals of specific objects of finite rank. Those objects have the form described in the following theorem, Golyandina and Usevich (2009); Golyandina et al. (2015).

Theorem 1 *And infinite 2D-array $\{x(n, m)\}_{n, m \in \mathbb{N}}$ is of finite rank if and only if*

$$x(n, m) = \sum_{k=1}^K p_k(n, m) \rho_{1k}^m \rho_{2k}^n \cos(2\pi(\omega_{1k}n + \omega_{2k}m) + \phi_k), \quad n, m \in \mathbb{N}, \quad (2)$$

where $p_k(n, m)$ are polynomials in n and m variables, $\rho_{\cdot k}$ are the damping factors, $\omega_{\cdot k}$ the frequency parameters and ϕ_k are the phase parameters.

2.2 ESPRIT

Estimation of Signal Parameters via Rotational Invariance Techniques (ESPRIT) is a method to estimate parameters of a mixture of one-dimensional, Roy and Kailath (1989), and two-dimensional amplitude-modulated sinusoids, Rouquette and Najim (2001); Wang et al. (2005), in background noise.

For the 2D-ESPRIT method, Rouquette and Najim (2001), the observed data y is generated by the following additive model:

$$y(m, n) = x(m, n) + \varepsilon(m, n), \quad (3)$$

where $0 \leq m \leq N_x - 1$ and $0 \leq n \leq N_y - 1$, ε is the zero-mean Gaussian noise with variance σ^2 . The model for the signal x is given by the sum of amplitude modulated two-dimensional sinusoid

$$x(m, n) = \sum_{k=1}^K s_k \rho_{1k}^m \rho_{2k}^n \cos(2\pi(\omega_{1k}m + \omega_{2k}n) + \phi_k), \quad (4)$$

where ω_{1k}, ω_{2k} are the normalised frequencies in different directions, α_{1k}, α_{2k} are the damping factors, s_k amplitudes, and ϕ_k phases.

By Theorem 1 the signal (4) is of finite rank. The ESPRIT methods utilises the fact of the rank-deficiency of the trajectory matrix of the observed signal y , and a certain transformation matrix between sub-trajectory matrices is obtained. The frequency and damping factor parameters are computed from the argument and absolute values of the complex-valued eigenvalues of the obtained transformation matrix. See more details in Roy and Kailath (1989); Rouquette and Najim (2001).

2.3 Amplitude, phase estimation

The ESPRIT estimates the frequencies $\omega_{\cdot k}$ and the damping factors $\rho_{\cdot k}$ of the signal model (4). Here only the amplitudes s_k and phases ϕ_k remain to be estimated. This problem can be reformulated as a linear regression model using the formula of the cosine of sums. With this formula, (4) can be rewritten as

$$x(m, n) = \sum_{k=1}^K A_k \rho_{1k}^m \rho_{2k}^n \cos(2\pi(\omega_{1k}n + \omega_{2k}m)) - B_k \rho_{1k}^m \rho_{2k}^n \sin(2\pi(\omega_{1k}n + \omega_{2k}m)), \quad (5)$$

where $\rho_{\cdot k}, \omega_{\cdot k}$ are the parameters estimated from the ESPRIT, and A_k, B_k are the parameters of the linear model to be estimated.

Note that the dependent variable in the linear regression model are the values of $x(n, m)$, the finite-rank signal extracted from y . In terms of the SSA algorithm this corresponds to the series reconstructed from the selected components.

The amplitude and phase are given by:

$$s_k = \sqrt{A_k^2 + B_k^2}, \quad \phi_k = \text{atan}(B_k/A_k). \quad (6)$$

2.4 Implementation. Comparison to alternatives methods

For our application, we use an R-package ‘‘Rssa’’, Golyandina et al. (2018); Korobeynikov (2010); Golyandina and Korobeynikov (2014); Golyandina et al. (2015), where all the required functionality including the ESPRIT method is implemented. It should be noted that the trajectory matrix for 2D-SSA is large and has $O(N^2)$ number of elements, where N is a number of pixels in the signal image. However, the structure of the Hankel-block-Hankel matrix allows implementing of SVD with Lanczos algorithm efficiently in time and memory by computing product of a matrix and a vector with Fast Fourier Transform, Korobeynikov (2010); Lanczos (1950).

For computing amplitude and phase parameters, we utilise a standard R-function ‘‘lm’’, Chambers (1992).

The form of the parametric model of the SSA signal suggests that Fourier analysis can be used to obtain similar results. However, in order to obtain a compact representation of a signal a small Fourier coefficient should be discarded. For that purpose a sparse Fourier analysis approach can be used, Hassanieh et al. (2012).

However, the parametric model of the SSA signal is more flexible, as every periodic has an amplitude modulation. Furthermore, the Fourier analysis is a low-resolution type method, as in the context of time series, frequency can be estimated only up to $1/N$, where N is the length of the time series. Whereas ESPRIT is regarded as a high-resolution method.

3 Data

In this section we discuss the data that is used in this paper. The data was acquired within the framework of the PEARL-TF project. The PEARL-TF (2020) website contains detailed information about the project and the involved partners. In this project, the data from several solar parks with thin-film modules were collected. In addition to EL images, also performance characteristics of the modules were measured.

The EL images are taken at predefined conditions (selected fixed applied current and/or fixed applied voltage). A silicon CCD sensor camera is used to measure subsequently several parts of the module, with the images being stitched afterwards. The applied voltage and the applied current together with the temperature of the module are being recorded. The I/V characteristics are also measured and the solar cell performance parameters are determined.

The database contains over 9500 EL images of thin-film PV modules. The bulk of these EL images (about 6000) are from co-evaporated Copper Indium Gallium di-Selenide (CIGS) modules with a chemical bath Cadmium Sulfide buffer. All EL images shown in this work are from such CIGS modules. Every image is supplied with measured performance data. A typical EL image of a thin-film module from our database is depicted in Figure 1. The module consists of 150 connected cells in series (in Figure 1 the cells are recognised as horizontal stripes). The cells are separated by interconnection lines (horizontal dark lines in Figure 1). In addition, the module is separated into 5 parallel sub-modules by vertical isolation lines (dark vertical lines).

Every EL image consists of several stitched images. Different stitched parts of the image have different overall intensities (see Figure 1). This is attributed to the metastable behaviour of thin-film solar cells, where the electrical properties of the cell can change during the measurement.

4 Results

In this section we discuss a selection of image processing methods that we build on top of the SSA framework.

Firstly, Section 4.1 describes a decomposition of EL images into several components: global intensity, cell, and aperiodic components. This is a direct result of the SSA decomposition, where grouping is performed using prior knowledge of the image size and number of cells in a module.

Secondly, a parametric model of the cell component signal is used to achieve several goals. The symbolic differentiation allows a global search for the minimum points in the cell components, that can be used to identify the interconnection lines (Section 4.2). Furthermore, we demonstrate the estimation of the inverse characteristic length, a physical parameter that depends on several resistances in a PV module (Section 4.3).

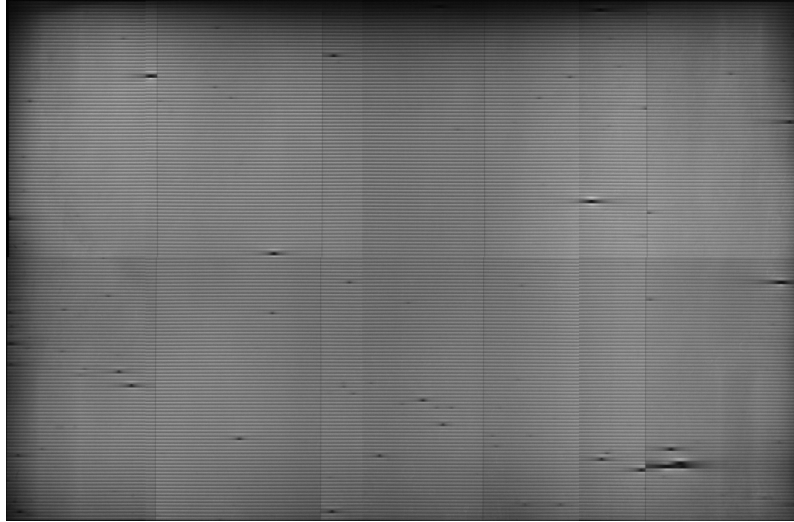


Fig. 1: Thin-film module EL image. A module consists of 150 cells (positioned horizontally) connected in series. The cells are separated by interconnection lines (horizontal dark lines). The module consists of several submodules separated by vertical isolation lines, which appear dark in the EL image. The EL image is stitched (there are 1 horizontal and 3 vertical stitch lines); overall intensities of different patches of images are different. These intensity differences are attributed to metastable changes during the measurement.

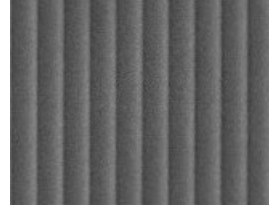
Lastly, MSSA and its parametric model is used to obtain a non-linear transformation needed to correct the stitch line in EL images.

4.1 Image decomposition

The grouping step of the SSA algorithm allows combining of decomposed rank-one components into groups. We define these groups that result in EL image decomposition onto 3 components: global intensity variation, cell, and aperiodic components.

Figure 2 shows a close up image of the module, that clearly identifies a set of 10 parallel cells separated by interconnection lines. The EL intensity varies systematically over the cell width. This is the result of the series resistance of the electrodes. As the transparent zinc-oxide front electrode exhibits a much larger sheet resistance than the molybdenum back contact, the voltage over the diode junction drops from one side to the other Helbig et al. (2010); Pieters and Rau (2015). As the EL intensity depends primarily on the cell voltage this leads to a clear intensity gradient over each cell.

Fig. 2 An enlargement of a 10-cells EL image region. Each cell exhibit periodic behaviour.



To achieve good separability of the periodic components, the parameter L of the SSA embedding is selected to equal approximately half of the dimensions of the input image, Golyandina et al. (2001, 2018). The ESPRIT estimates frequencies and damping factors of the components, which are used in the decision of the grouping step.

A thin-film module consists of a fixed number of interconnected cells, therefore, the cell components can be identified as periodic components that have a period smaller than $\frac{\text{image width}}{150}$. The other components are grouped together as the global variation and the residual image captures information of non-low rank signals, such as aperiodic features of an EL image.

The image decomposition algorithm steps are described in the Algorithm 1.

Input: EL image X with dimensions $N_x \times N_y$.

Output: Three images with the same dimensions as X : global intensity component G , cell component S and aperiodic component R .

1. Perform embedding and decomposition steps of the 2D-SSA algorithm for X . Compute first 50 elements in the rank-one decomposition of SVD, denote the sum of this components as $\tilde{\mathbf{X}}$.
2. Apply ESPRIT on the low-rank signal $\tilde{\mathbf{X}}$.
3.
 - Set the cell components S as in (4), choosing only periodics with frequency $\omega_{1k} > \frac{150}{N_x}$.
 - The global intensity component G is composed from components of non-periodics and periodics with frequency $\omega_{1k} < \frac{150}{N_x}$.
 - The $R := X - S - G$.

Algorithm 1: EL image decomposition

The choice of the 50 computed components is arbitrary, as 10 components incorporate 99.9% of the Frobenius norm of the trajectory matrix \mathbf{X} . The RMSE of the linear regression model in the ESPRIT indicates the accuracy of the model (4). For a set of 50 EL images, the mean RMSE equals 0.033.

Figure 3 depicts the non-cell components, the cell components, and the residual image. It can be argued that different components have a different physical origin. By its nature, the global variation component describes changes in a material which results in large losses that spread over large portions of a module. The cell component variation is influenced by the EL measurement conditions. Lastly, the aperiodic component captures effects caused by non-regular changes in material like shunts, or droplets (see Sovetkin et al. (2021)).

Shunts are characterized by a more conductive connection between the front and back electrodes than the normal solar cell structure (i.e. the solar cell structure is damaged or missing). There are many causes for shunts. Commonly shunts originate from debris of the copper evaporation source or pinholes in the CIGS absorber Mistic et al. (2015); Mistic (2017). Shunts are generally relevant to the solar module performance, in particular under low light conditions Weber et al. (2011).

In addition to shunts we noticed the CIGS modules often exhibit “droplets” in the EL images. The appearance of droplets resembles water stains and thus we speculate these structures originate from the chemical bath deposition. At this point it is unknown what the impact of droplets is on the module performance, however, the bright appearance imply a local change in quantum efficiency according to the reciprocity relations between luminescence and quantum efficiency Rau (2007).

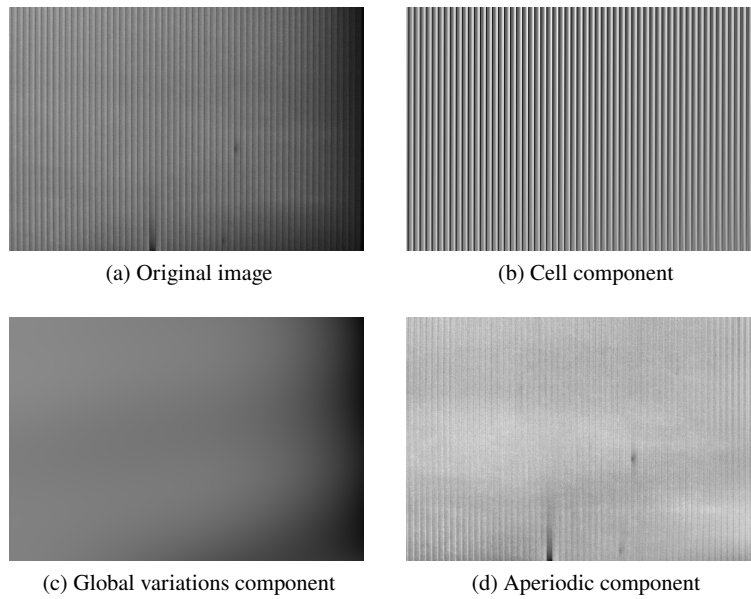


Fig. 3: Decomposition of an EL image onto 3 components

We remark that decomposition can be applied to an image (additive model assumption) as well as to the logarithm of an image (multiplicative model assumption). The logarithm of an image corresponds to the internal voltage (see (8), Section 4.3).

Furthermore, we remark that it is important to correct any perspective distortion present in images, as a periodic image distorted in such a way is no longer a signal with a finite rank in the settings of the 2D-SSA methodology.

4.2 Interconnection line detection

In order to identify interconnection lines, it is sufficient to locate the global minima for every level in the normal direction of the interconnection lines.

The ESPRIT model satisfies equation (4), which is a sum of amplitude-modulated cosine functions. A derivative of such function is again a sum of polynomial amplitude-modulated cosine functions, similar to the general form of the signal of finite rank (2). Such derivatives can be computed symbolically. Hence all the global minima in the normal direction of the interconnection lines can be identified by evaluating precise values of the derivatives, and filtering out points that satisfy a minima extreme point requirement.

Algorithm 2 describes the steps of the interconnection line identification. Symbolic derivatives are computed using the “Deriv” R-package, Clausen and Sokol (2019).

Input:

- EL image with dimensions $N_x \times N_y$.
- Regular mesh of points $P = \{n, m \in \mathbb{R}, 1 \leq n \leq N_x, 1 \leq m \leq N_y\}$.

Output: Array of coordinates $O \subset P$, corresponding to the estimated locations of interconnection lines.

1. Compute EL image decomposition with Algorithm 1.
2. Use ESPRIT and linear regression to estimate parameters of the model (4), see Sections 2.2 and 2.3. Denote the resulting signal as $S : P \rightarrow \mathbb{R}$.
3. Compute symbolically expression for derivative $dS := \frac{\partial S}{\partial m} : P \rightarrow \mathbb{R}$.
4. The output set $O := \{p \in P : dS(p-) < 0 \text{ and } dS(p+) > 0\}$, where $p-, p+$ are the neighbours in P of the point p in the m -variable direction.

Algorithm 2: Interconnection line detection

We remark that the resulting expression for the cell component signal, as well as its derivatives, can be computed on a finer grid P than the original pixel coordinates. Hence the interconnection line identification is performed with sub-pixel accuracy.

Figure 4 visually demonstrates the steps of the method. Figure 4a displays the estimated cell component. Figure 4b shows a slice of a pixel value intensities in Figure 4a, where computed local minima identified with red dots. Lastly, Figure 4c shows the module with its interconnection lines identified by red lines.

4.3 Inverse characteristic length estimation

Another application of the obtained parametric expression for a module is an estimation of the inverse characteristic length λ Helbig et al. (2010); Pieters and Rau (2015).

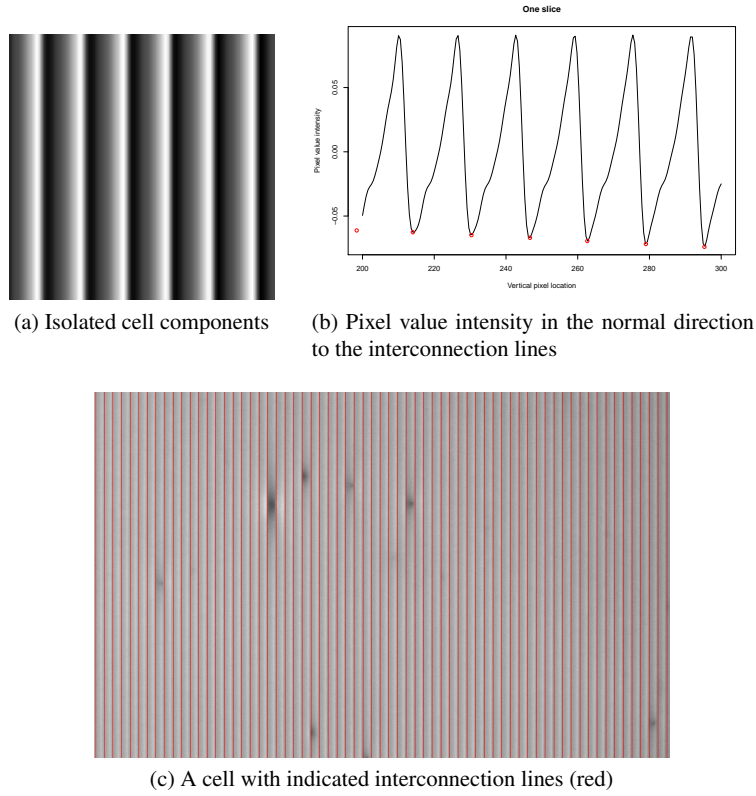


Fig. 4: Detection of the interconnection lines

In a defect-free PV module, there are no currents in the vertical direction (along the interconnection line direction), and thus current satisfies the following linearised 1D Poisson equation, Helbig et al. (2010); Augarten et al. (2016).

$$\frac{\partial^2 V}{\partial x^2} = \lambda^2 V, \quad (7)$$

where $\lambda = \sqrt{\frac{R_{\text{sheet}}}{r_j}}$ is the inverse characteristic length, where R_{sheet} is the sheet resistance and r_j is the local differential junction resistance. Note, that (7) is an equation between two fields, where $V(x, y)$ and $\lambda(x, y)$ depend on the position (x, y) in a PV module.

The luminescence intensity related to the internal voltage via the following relation

$$I = c \exp(V/c_0) \implies V = \frac{1}{c_0} \ln(I/c), \quad (8)$$

where the constant $c_0 = \frac{q}{kT}$ is the thermal voltage (with the elementary charge, q , Boltzmann's constant, k , and the temperature, T), c is a parameter that describes the optical system from the photon generation in the solar cell absorber material to the photon detection within the camera. As such the parameter c depends on the quantum efficiency of both the solar cell and the used camera including all optical components, and the spectral photon density of a black body Rau (2007). Generally, the constant c may vary over the solar cell area due to the camera optics and variations in the solar cell properties. However, in general, the variations in c are small compared to the exponential voltage-dependency Abou-Ras et al. (2016). In our analysis, we assume that c is constant over the whole module area, and is accessible to a researcher.

The decomposition of a signal onto trend and cell components provides us an EL image signal without small aperiodic defects like shunts (small dark areas within cells boundaries). The global intensity and cell components without small aperiodic defects can be considered as a module without defects. Hence, we consider a module without defects to be an image $G + S$, of the output of Algorithm 1.

Hence combining (7) and (8), allows us to express inverse characteristic length as a function of intensity and its derivative:

$$\frac{\partial^2 V}{\partial x^2} = \frac{\frac{\partial^2 I}{\partial x^2} I - \left(\frac{\partial I}{\partial x}\right)^2}{c_0 I^2}, \quad (9)$$

and therefore,

$$\lambda^2 = \frac{\frac{\partial^2 I}{\partial x^2} I - \left(\frac{\partial I}{\partial x}\right)^2}{I^2 \ln(I/c)}. \quad (10)$$

All derivatives are computed symbolically from the estimated cell component signal.

4.4 Stitched image correction

In order to achieve higher image resolution, several EL images can be stitched together. However, the image aligning can be imperfect, as shown in Figure 5a. These misaligned image patches and the resulting stitch line can be attributed to incorrect perspective as well as radial distortions. The latter distortion leads to a non-linear transformation that is needed to be applied to an image for the stitch line correction.

Algorithm 3 proposes an approach to correct such distortion. The basic idea of the algorithm is the estimation of phase shifts in neighbouring locations, where each shift is estimated by application of MSSA, Golyandina et al. (2018), in a direction perpendicular to the interconnection lines.

The result of the algorithm is a displacement map that defines shifts in the horizontal direction. Note that shifts have sub-pixel accuracy.

Input: EL image X with dimensions $N_x \times N_y$.

Output: A displacement map M , a vector of dimension $N_x - 1$ indicating size of horizontal shifts in image X (except for the first row).

1. For each image row i starting from the second row:
 - a. Compute MSSA of the i and $i - 1$ row of the image I .
 - b. Estimate the ESPRIT parameters.
 - c. Filter out periods not corresponding to cell components. Let cell component indices be I .
 - d. Compute shift for cell each component $s_k := \frac{\phi_k}{2\pi\omega_k}$, $k \in I$.
2. Set $M_i := \max_{k \in I} s_k$.

Algorithm 3: Stitched image correction

Figure 5 shows the result of the algorithm. Figure 5a shows a patch of the original EL image with a stitched part. Figure 5b depicts the shifted image, resulting from applying the displacement map. As each displacement is estimated locally between neighbours, the resulting transformation is a non-linear transformation.

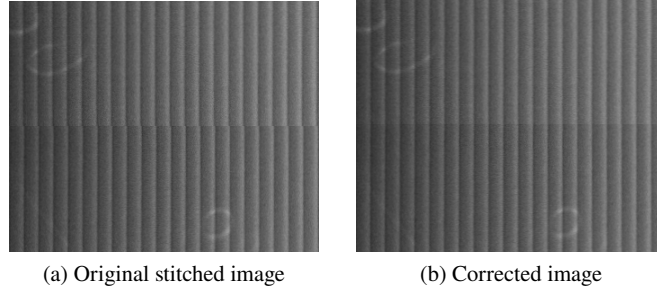


Fig. 5: An example of the stitched image correction

To evaluate the accuracy of the phase shift estimation we model the following two time series

$$s_1(x) = \cos(2\pi x/50) + \cos(2\pi x/20) + \cos(2\pi x/30) + \varepsilon_1(x), \quad (11)$$

$$s_2(x) = 2 \cos(2\pi x/70) + \underbrace{\cos(2\pi(x+7)/20) + \cos(2\pi(x+7)/30)}_{\text{signal}} + \varepsilon_2(x), \quad (12)$$

(13)

where $x \in \{1, 2, \dots, 1000\}$, periodics with period 20 and 30 correspond to the signal (models the cell component), periodics with period 50 and 70 slowly varying trend, and $\varepsilon_1, \varepsilon_2$ are two independent Gaussian iid processes with zero-mean and unit variance.

The signal part of the series s_1 is shifted by 7 units relative to the signal of the series s_2 . Figure 6 shows a part of those series on the interval $[1, 100]$.

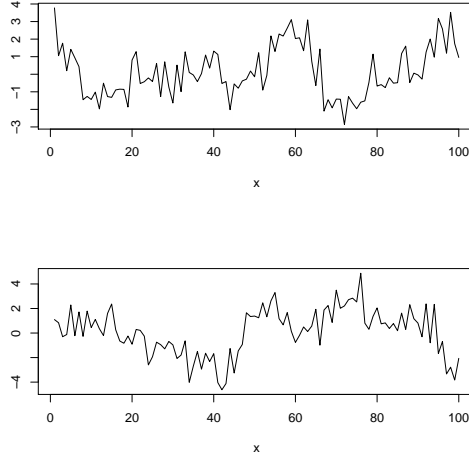


Fig. 6 $s_1(x)$ and $s_2(x)$ time series, for $x \in [1, 100]$. The signal (periodics with periods 20 and 30) are “hidden” with a trend and a noise components

Table 1 shows the accuracy of the shift estimation of the selected signal components. That simulation was performed using 100 repetitions.

Table 1: Accuracy of the shift estimation between signals in time series s_1 and s_2

RMSE	Estimate mean	25% quantile	75% quantile
0.248	7.003	6.836	7.160

5 Conclusions

In this paper we demonstrated an application of SSA on EL images of thin-film PV modules. This low-rank approach allows capturing several important aspects of those images, namely, global and local repetitive variations (or cell components) in an EL image.

Several image processing algorithms based on parametric models of SSA are proposed. The first method identified the interconnection lines between the individual cells at sub-pixel accuracy, and the second method corrects the incorrectly stitched images.

Furthermore, we propose an approach based on symbolic differentiation of the SSA signal to estimate the so-called inverse characteristic length, a physical parameter of a module.

We note that in the settings of 2D-SSA it is important to correct perspective distortion in such EL images. The two-dimensional cosine array transformed with perspective distortion is no longer a finite-rank signal.

It should be noted that the information captured by SSA is not complete, as local aperiodic features, such as shunts and droplets are not signals of finite rank. Therefore, the full analysis of such PV modules requires other methods. For example, we complement the signal captured by SSA using an encoder-decoder segmentation approach of individual defects (see Sovetkin et al. (2021, 2020)).

Lastly, we remark that source code and a sample of EL images data are available upon request.

Acknowledgements This work is supported by the Solar-era.net framework in the project ‘‘PEARL TF-PV’’ (Förderkenzeichen: 0324193A) and partly funded by the HGF project ‘‘Living Lab Energy Campus (LLEC)’’.

Appendix

2D-SSA embedding and projection

Following notations of Golyandina and Usevich (2010), let x be an 2D-array with dimensions $(N_x, N_y) \in \mathbb{N}^2$:

$$x = \begin{pmatrix} x(0,0) & x(0,1) & \dots & x(0, N_y-1) \\ x(1,0) & x(1,1) & \dots & x(1, N_y-1) \\ \vdots & \vdots & \ddots & \vdots \\ x(N_x-1,0) & x(N_x-1,1) & \dots & x(N_x-1, N_y-1) \end{pmatrix}. \quad (14)$$

The 2D-SSA embedding is defined by the window size vector (L_x, L_y) , which is restricted by $1 \leq L_x \leq N_x, 1 \leq L_y \leq N_y$, and $1 < L_x L_y < N_x N_y$. Let $K_x := N_x - L_x + 1$ and $K_y := N_y - L_y + 1$, then the trajectory matrix of 2D-SSA is given by the following Hankel-block-Hankel matrix:

$$\mathbf{X} := \begin{pmatrix} \mathbf{X}_0 & \mathbf{X}_1 & \mathbf{X}_2 & \dots & \mathbf{X}_{K_y-1} \\ \mathbf{X}_1 & \mathbf{X}_2 & \mathbf{X}_3 & \dots & \mathbf{X}_{K_y} \\ \mathbf{X}_2 & \mathbf{X}_3 & \ddots & \ddots & \vdots \\ \vdots & \vdots & \ddots & \ddots & \vdots \\ \mathbf{X}_{L_y-1} & \mathbf{X}_{L_y} & \dots & \dots & \mathbf{X}_{N_y-1} \end{pmatrix}, \quad (15)$$

where each block

$$\mathbf{X}_i := \begin{pmatrix} x(0, i) & x(1, i) & \dots & x(K_x - 1, i) \\ x(1, i) & x(2, i) & \dots & x(K_x, i) \\ \vdots & \vdots & \ddots & \vdots \\ x(L_x - 1, i) & x(L_x, i) & \dots & x(N_x - 1, i) \end{pmatrix}. \quad (16)$$

By construction there is a one-to-one correspondence between 2D-arrays of size $N_x \times N_y$ and the Hankel-block-Hankel matrices.

Let \mathbf{Z} be an arbitrary matrix with a block-structure, where each block \mathbf{Z}_i has the same dimension as the matrix \mathbf{X}_i

$$\mathbf{Z} = \begin{pmatrix} \mathbf{Z}_0 & \mathbf{Z}_1 & \mathbf{Z}_2 & \dots & \mathbf{Z}_{K_y-1} \\ \mathbf{Z}_1 & \mathbf{Z}_2 & \mathbf{Z}_3 & \dots & \mathbf{Z}_{K_y} \\ \mathbf{Z}_2 & \mathbf{Z}_3 & \ddots & \ddots & \vdots \\ \vdots & \vdots & \ddots & \ddots & \vdots \\ \mathbf{Z}_{L_y-1} & \mathbf{Z}_{L_y} & \dots & \dots & \mathbf{Z}_{N_y-1} \end{pmatrix}. \quad (17)$$

Then a projection of \mathbf{Z} to Hankel-block-Hankel matrix can be computed in two steps. Firstly, diagonal averaging is performed within blocks $\mathbf{Z}_i, i \in 0, \dots, N_y - 1$. Secondly, the blocks of the matrix \mathbf{Z} are averaged between themselves. The projection can be applied in the reverse order as well.

SVD

Let $\mathbf{S} = \mathbf{X}\mathbf{X}^T$, $\lambda_1 \geq \dots \geq \lambda_d > 0$ be non-zero eigenvalues of the matrix \mathbf{S} , U_1, \dots, U_d be the corresponding eigenvectors, and $V_i := \mathbf{X}^T U_i / \sqrt{\lambda_i}, i = 1, \dots, d$.

Then SVD of the matrix \mathbf{X} can be written as

$$\mathbf{X} = \mathbf{X}_1 + \dots + \mathbf{X}_d. \quad (18)$$

The values $\sqrt{\lambda_i}$ are the singular values of \mathbf{X} .

Finite-rank signal

An image x has rank r if the rank of trajectory matrix \mathbf{X} equals $r < \min(L_x, L_y, K_y, K_x)$. In other words, the trajectory matrix is rank-deficient. If rank r does not depend on the choice of L for any sufficiently large dimensions of x , then x is called to have a *finite rank*.

Objects of finite rank are closely related to the linear recurrent sequences, Kurakin et al. (1995). Linear recurrent formulae are used to build forecast based on the SSA signal.

Computational complexity

From the computational point of view, the hardest steps of the proposed algorithms are the singular value decomposition (SVD), ESPRIT (Section 2.2), and the phase and amplitude least-squares fit (Section 2.3).

In the context of the SSA application, the computational complexity of the SVD of a Hankel-block-Hankel matrix is $O(kN \log N + k^2 N)$, where N is the number of pixels in an image and k is the number of computed eigentriples, Korobeynikov (2010). The linear equations solved for ESPRIT and the phase and amplitude parameters estimations are solved using QR-decomposition, and require $O(N^3)$ operations. Our numerical experiments show that the SVD decomposition dominates the computational time for the proposed algorithms for image sizes with width and height less than 4000 pixels.

To measure the required time and memory of the proposed algorithms we utilise a machine with Intel(R) Xeon(R) CPU E5-1620 3.5GHz processor and 31GB of RAM. The time measurements are performed on a single CPU.

Figure 7 shows the time required to perform steps of Algorithm 1 for square images (width equals height) for different image widths. The red points correspond to the measured time in seconds, and the black line is a parabola fitted to the points. Table 2 shows the amount of memory required for the steps of Algorithm 1.

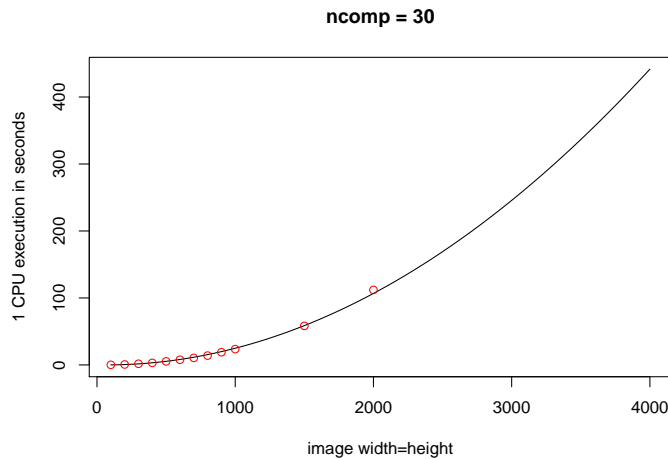


Fig. 7: Computation time required for Algorithm 1 for different input image sizes.

Algorithm 2 utilises results of the Algorithm 1 and requires additional symbolical differentiation. Such computation is also required for the inverse characteristic length (Section 4.3). The running time of the symbolical differentiation depends on the

Table 2: Maximum memory required for Algorithm 1 for different input image sizes.

Image width and height	500	1000	1500	2000
Maximum RAM in GB	0.5	1.6	3.2	5.5

number of terms of the signal (4). Table 3 demonstrates the relationship between the number of terms in the signal and the running time required for the symbolic differentiation. Algorithm 2 and the inverse characteristic length computation works with the cell component that typically consists of 5–7 terms.

Table 3: Running time of the symbolical differentiation routine used in Algorithm 2 and the inverse characteristic length estimation in Section 4.3

Number of components	5	9	13	17
Execution time in seconds	0.15	0.46	1.27	1.79

Algorithm 3 utilises a different version of SSA, that requires less time and memory, however, the algorithm computes MSSA multiple times for several pairs of neighbour rows. A single iteration of the algorithm loop requires 0.7 seconds and 0.78 of RAM for an image with width of 4000 pixels. Different iterations of the loop can be run in parallel. Note that most of the used memory is occupied by an image itself, and hence the memory can be shared by multiple processes. Algorithm 3 usually requires running about 100–200 iterations, as an approximate location of the stitching lines is known. Hence, the total running time an 8-core processor can be as little as 20 seconds.

Lastly, we remark the proposed algorithms run in a deterministic amount of time. Hence, the methods can be run in real-time applications.

References

- Abou-Ras D, Kirchartz T, Rau U (2016) Advanced characterization techniques for thin film solar cells. John Wiley & Sons
- Augarten Y, Wrigley A, Rau U, Pieters B (2016) Calculation of the TCO sheet resistance in thin film modules using electroluminescence imaging. In: 2016 IEEE 43rd Photovoltaic Specialists Conference (PVSC), IEEE, pp 1527–1531
- Broomhead D, King G (1986) Extracting qualitative dynamics from experimental data. *Physica D: Nonlinear Phenomena* 20(2–3):217–236
- Chambers JM (1992) Linear models. *Statistical models in S*
- Clausen A, Sokol S (2019) Deriv: R-based Symbolic Differentiation. URL <https://CRAN.R-project.org/package=Deriv>, deriv package version 4.0

- Colebrook J (1982) Continuous plankton records-phytoplankton, zooplankton and environment, northeast atlantic and north-sea, 1958-1980. *Oceanologica Acta* 5(4):473–480
- Danilov D, Zhigljavsky A (1997) Principal components of time series: the “Caterpillar” method. St Petersburg: University of St Petersburg pp 1–307
- Deutsch S, Buerhop-Lutz C, Maier A, Gallwitz F, Riess C (2018) Segmentation of photovoltaic module cells in electroluminescence images. arXiv preprint arXiv:180606530
- Deutsch S, Christlein V, Berger S, Buerhop-Lutz C, Maier A, Gallwitz F, Riess C (2019) Automatic classification of defective photovoltaic module cells in electroluminescence images. *Solar Energy* 185:455–468
- Demant M, Virtue P, Kovvali AS, Yu SX, Rein S (2018) Deep learning approach to inline quality rating and mapping of multi-crystalline si-wafers. In: 35th European Photovoltaic Solar Energy Conference and Exhibition, pp 814–818
- Elsner JB, Tsonis AA (1996) *Phase Space Reconstruction*, Springer US, Boston, MA, pp 143–155. DOI 10.1007/978-1-4757-2514-8_10, URL https://doi.org/10.1007/978-1-4757-2514-8_10
- Fraedrich K (1986) Estimating the dimension of weather and climate attraction. *Journal of Atmosphere Science* 43:419–432
- Golyandina N, Korobeynikov A (2014) Basic singular spectrum analysis and forecasting with R. *Computational Statistics and Data Analysis* 71:934–954, r package version 1.0
- Golyandina N, Usevich K (2009) An algebraic view on finite rank in 2d-ssa. In: *Proceedings of the 6th St.Petersburg Workshop on Simulation*, pp 308–313
- Golyandina N, Usevich K (2010) 2D-extension of singular spectrum analysis: algorithm and elements of theory. In: *Matrix Methods: Theory, Algorithms and Applications: Dedicated to the Memory of Gene Golub*, World Scientific, pp 449–473
- Golyandina N, Nekrutkin V, Zhigljavsky A (2001) *Analysis of time series structure: SSA and related techniques*. Chapman and Hall/CRC
- Golyandina N, Korobeynikov A, Shlemov A, Usevich K (2015) Multivariate and 2D extensions of singular spectrum analysis with the Rssa package. *Journal of Statistical Software* 67(2):1–78, DOI 10.18637/jss.v067.i02
- Golyandina N, Korobeynikov A, Zhigljavsky A (2018) *Singular Spectrum Analysis with R*. Springer
- Groth A, Ghil M (2015) Monte carlo singular spectrum analysis (SSA) revisited: Detecting oscillator clusters in multivariate datasets. *Journal of Climate* 28(19):7873–7893
- Hassanieh H, Indyk P, Katabi D, Price E (2012) Simple and practical algorithm for sparse fourier transform. In: *Proceedings of the twenty-third annual ACM-SIAM symposium on Discrete Algorithms*, Society for Industrial and Applied Mathematics, pp 1183–1194
- Helbig A, Kirchartz T, Schaeffler R, Werner JH, Rau U (2010) Quantitative electroluminescence analysis of resistive losses in Cu (In, Ga) Se₂ thin-film modules. *Solar Energy Materials and Solar Cells* 94(6):979–984

- Holloway DM, Lopes FJ, da Fontoura Costa L, Travençolo BA, Golyandina N, Usevich K, Spirov AV (2011) Gene expression noise in spatial patterning: hunchback promoter structure affects noise amplitude and distribution in drosophila segmentation. *PLoS Comput Biol* 7(2):e1001069
- Karimi AM, Fada JS, Hossain MA, Yang S, Peshek TJ, Braid JL, French RH (2019) Automated pipeline for photovoltaic module electroluminescence image processing and degradation feature classification. *IEEE Journal of Photovoltaics* 9(5):1324–1335
- Köntges M, Kurtz S, Packard C, Jahn U, Berger K, Kato K, Friesen T, Liu H, Van Iseghem M (2015) Iea-pvps t13-01 2014 review of failures of photovoltaic modules final. Tech. rep., Technical Report IEA-PVPS T13-01: 2014, IEA-PVPS Task 13
- Korobeynikov A (2010) Computation- and space-efficient implementation of SSA. *Statistics and Its Interface* 3(3):357–368, r package version 1.0
- Kurakin V, Kuzmin A, Mikhalev A, Nechaev A (1995) Linear recurring sequences over rings and modules. *Journal of Mathematical Sciences* 76(6):2793–2915
- Lanczos C (1950) An iteration method for the solution of the eigenvalue problem of linear differential and integral operators. United States Governm. Press Office Los Angeles, CA
- Lima G, et al. (2016) Gap filling of precipitation data by SSA-singular spectrum analysis. In: *Journal of Physics: Conference Series*, IOP Publishing, vol 759, p 012085
- Mamou J, Feleppa EJ (2007) Singular spectrum analysis applied to ultrasonic detection and imaging of brachytherapy seeds. *The Journal of the Acoustical Society of America* 121(3):1790–1801
- Markovsky I (2018) *Low-Rank Approximation*, vol 139. Springer
- Misic B (2017) Analysis and Simulation of Macroscopic Defects in Cu(In,Ga)Se₂ Photovoltaic thin film modules, *Schriften des Forschungszentrums Jülich. Reihe Energie und Umwelt / Energy and Environment*, vol 372, Forschungszentrum Jülich GmbH, pp 17–36
- Misic B, Pieters BE, Schweitzer U, Gerber A, Rau U (2015) Defect diagnostics of scribing failures and cu-rich debris in cu(in,ga)se₂ thin-film solar modules with electroluminescence and thermography. *IEEE Journal of Photovoltaics* 5(4):1179–1187, DOI 10.1109/JPHOTOV.2015.2422143
- Monadjemi A (2004) Towards efficient texture classification and abnormality detection. PhD thesis, University of Bristol
- de Oliveira AKV, Aghaei M, Rüther R (2019) Automatic fault detection of photovoltaic array by convolutional neural networks during aerial infrared thermography. In: *36th European Photovoltaic Solar Energy Conference and Exhibition PEARL-TF* (2020) PEARL-TF project website. URL <https://pearl.tf.eu/>, accessed: 2020-09-01
- Pieters BE, Rau U (2015) A new 2d model for the electrical potential in a cell stripe in thin-film solar modules including local defects. *Progress in Photovoltaics: Research and Applications* 23(3):331–339, DOI 10.1002/pip.2436,

- URL <https://onlinelibrary.wiley.com/doi/abs/10.1002/pip.2436>,
<https://onlinelibrary.wiley.com/doi/pdf/10.1002/pip.2436>
- Qiao T, Ren J, Wang Z, Zabalza J, Sun M, Zhao H, Li S, Benediktsson JA, Dai Q, Marshall S (2016) Effective denoising and classification of hyperspectral images using curvelet transform and singular spectrum analysis. *IEEE transactions on geoscience and remote sensing* 55(1):119–133
- Rau U (2007) Reciprocity relation between photovoltaic quantum efficiency and electroluminescent emission of solar cells. *Phys Rev B* 76:085303, DOI 10.1103/PhysRevB.76.085303, URL <https://link.aps.org/doi/10.1103/PhysRevB.76.085303>
- Rodriguez-Aragon LJ, Zhigljavsky A (2010) Singular spectrum analysis for image processing. *Statistics and Its Interface* 3(3):419–426
- Rouquette S, Najim M (2001) Estimation of frequencies and damping factors by two-dimensional ESPRIT type methods. *IEEE Transactions on signal processing* 49(1):237–245
- Roy R, Kailath T (1989) ESPRIT-estimation of signal parameters via rotational invariance techniques. *IEEE Transactions on acoustics, speech, and signal processing* 37(7):984–995
- Sella L, Vivaldo G, Groth A, Ghil M (2016) Economic cycles and their synchronization: A comparison of cyclic modes in three european countries. *Journal of Business Cycle Research* 12(1):25–48
- Shin PJ, Larson PE, Ohliger MA, Elad M, Pauly JM, Vigneron DB, Lustig M (2014) Calibrationless parallel imaging reconstruction based on structured low-rank matrix completion. *Magnetic resonance in medicine* 72(4):959–970
- Sovetkin E, Steland A (2019) Automatic processing and solar cell detection in photovoltaic electroluminescence images. *Integrated Computer-Aided Engineering (Preprint)*:1–15
- Sovetkin E, Pieters BE, Weber T, Achterberg EJ, Weeber A, Rau B, Rennhofer M, Theelen M (2020) PV-AIDED: Photovoltaic artificial intelligence defect identification. multichannel encoder-decoder ensemble models for electroluminescence images of thin-film photovoltaic modules, PEARL TF-PV. In: 37th EU PVSEC
- Sovetkin E, Weber T, Achterberg EJ, Pieters BE (2021) Encoder–decoder semantic segmentation models for electroluminescence images of thin-film photovoltaic modules. *IEEE Journal of Photovoltaics* 11(2):444–452, DOI 10.1109/JPHOTOV.2020.3041240
- Trickett S (2008) F-xy cadzow noise suppression. In: *SEG Technical Program Expanded Abstracts 2008*, Society of Exploration Geophysicists, pp 2586–2590
- Van Der Veen AJ, Deprettere EF, Swindlehurst AL (1993) Subspace-based signal analysis using singular value decomposition. *Proceedings of the IEEE* 81(9):1277–1308
- Vautard R, Ghil M (1989) Singular spectrum analysis in nonlinear dynamics, with applications to paleoclimatic time series. *Physica D: Nonlinear Phenomena* 35(3):395–424

- Wang Y, Chen JW, Liu Z (2005) Comments on " estimation of frequencies and damping factors by two-dimensional ESPRIT type methods". *IEEE transactions on signal processing* 53(8):3348–3349
- Weare BC, Nasstrom JS (1982) Examples of extended empirical orthogonal function analyses. *Monthly Weather Review* 110(6):481–485
- Weber T, Albert A, Ferretti N, Roericht M, Krauter S, Grunow P (2011) Electroluminescence investigation on thin film modules. In: 26th European Photovoltaic Solar Energy Conf.(26th EU PVSEC), pp 2584–2588
- Zabalza J, Ren J, Wang Z, Marshall S, Wang J (2014) Singular spectrum analysis for effective feature extraction in hyperspectral imaging. *IEEE Geoscience and Remote Sensing Letters* 11(11):1886–1890
- Zabalza J, Ren J, Zheng J, Han J, Zhao H, Li S, Marshall S (2015) Novel two-dimensional singular spectrum analysis for effective feature extraction and data classification in hyperspectral imaging. *IEEE transactions on geoscience and remote sensing* 53(8):4418–4433
- Zhigljavsky A (2010) Singular spectrum analysis for time series: Introduction to this special issue. *Statistics and its Interface* 3(3):255–258
- Zscheischler J, Mahecha M, et al. (2014) An extended approach for spatiotemporal gapfilling: Dealing with large and systematic gaps in geoscientific datasets. *Nonlinear Processes in Geophysics* 21(1):203–215